Evaluation of apatite silicates as solid oxide fuel cell electrolytes

D. Marrero-López [a,b,*], M.C. Martín-Sedeño [c], J. Peña-Martínez [b,d], J.C. Ruiz-Morales [b],
P. Núñez [b], M.A.G. Aranda [c], J.R. Ramos-Barrado [a]

[a] Dpto. de Física Aplicada I, Laboratorio de Materiales y Superficies (Unidad Asociada al C.S.I.C.), Universidad de Málaga, 29071 Málaga, Spain
[b] Dpto. de Química Inorgánica, Universidad de La Laguna, 38200 La Laguna, Tenerife, Spain
[c] Dpto. de Química Inorgánica, Universidad Málaga, 29071 Málaga, Spain
[d] Instituto de Energías Renovables, Parque Tecnológico, Universidad de Castilla La Mancha, 02006 Albacete, Spain

ARTICLE INFO

ABSTRACT

Apatite-type silicates have been considered as promising electrolytes for Solid Oxide Fuel Cells (SOFC); however studies on the potential use of these materials in SOFC devices have received relatively little attention. The lanthanum silicate with composition $La_{10}Si_{5.5}Al_{0.5}O_{26.75}$ has been evaluated as electrolyte with the electrode materials commonly used in SOFC, i.e. manganite, ferrite and cobaltite as cathode materials and NiO-CGO composite, chromium-manganite and Sr_2MgMoO_6 as anode materials. Chemical compatibility, area-specific resistance and fuel cell studies have been performed. X-ray powder diffraction (XRPD) analysis did not reveal any trace of reaction products between the apatite electrolyte and most of the aforementioned electrode materials. However, the area-specific polarisation resistance (ASR) of these electrodes in contact with apatite electrolyte increased significantly with the sintering temperature, indicating reactivity at the electrolyte/electrode interface. On the other hand, the ASR values are significantly improved using a ceria buffer layer between the electrolyte and electrode materials to prevent reactivity. Maximum power densities of 195 and 65 mWcm^{-2} were obtained at 850 and 700 °C, respectively in H_2 fuel, using an 1 mm-thick electrolyte, a NiO-$Ce_{0.8}Gd_{0.2}O_{1.9}$ composite as anode and $La_{0.6}Sr_{0.4}Co_{0.8}Fe_{0.2}O_{3-\delta}$ as cathode materials. This fuel cell was tested for 100 h in 5%H_2–Ar atmosphere showing stable performance.

© 2009 Elsevier B.V. All rights reserved.

1. Introduction

Solid Oxide Fuel Cells (SOFCs) are promising solid devices for the electrochemical conversion of a fuel directly into electrical power. Such devices render theoretical efficiencies significantly higher than those based on the combustion of fossil fuels [1,2]. Each single cell consists of three main ceramic components: an anode and a cathode separated by a solid electrolyte. The electrolyte must be an oxide ion conductor with negligible electronic contribution and it must be dense to prevent gas mixing. The anode and cathode should have good electronic conductivity, in addition to certain catalytic activity towards fuel oxidation and oxygen reduction, respectively. The cell components must have several requirements: chemical, morphological and dimensional stability in the corresponding gas-environment [1–4]. Furthermore, the ceramic components must be chemical and physically compatible to avoid

undesirable reactions that may lead to a decrease of the fuel cell efficiency.

Yttria-stabilised zirconia (YSZ) is the most commonly used SOFC electrolyte because it exhibits good thermal and chemical stability to operate at high temperatures, although the ionic conductivity is insufficient below 800 °C to achieve high efficiency [1,4]. The high operating temperatures also limit the election of compatible electrode and interconnect materials with this electrolyte. In this sense, several alternative oxide ion conductors have been investigated over the last few years, including doped CeO_2 [5–7], $LaGaO_3$-based perovskites [7,8] and LAMOX compounds derived from $La_2Mo_2O_9$ [9,10]. These phases exhibit higher ionic conductivity than YSZ in the intermediate temperature range (600–800 °C), but present some limitations that must be overcome before they become competitive compared to YSZ. In particular, the partial reduction of Ce^{4+} to Ce^{3+} in doped ceria produces an increase of the non-desirable n-type electronic conductivity and lattice expansion, which may lead to mechanical failure [5,7]. The applicability of lanthanum gallate is limited by: the formation of undesirable secondary phases during the synthesis; reactivity with NiO, which is commonly used in the anode; and volatilisation of gallium oxide at high temperatures and low oxygen partial pressures [1,2,11]. $La_2Mo_2O_9$-based electrolytes exhibit low redox stability under reducing conditions

Table 1
Composition, synthesis method, synthesis temperature (T_s), space group (s.g.) and cell parameters at room temperature for the different electrolyte and electrode materials.

Composition	Abbreviation	Synthesis	T_s (°C)	s.g.	Cell parameters (Å)
$La_{10}Si_{5.5}Al_{0.5}O_{26.75}$	Apatite	FD	1100	$P6_3/m$	$a = 9.7245(3), c = 7.2111(2)$
$La_{0.8}Sr_{0.2}MnO_{3-\delta}$	LSM	Praxair	–	$R\bar{3}c$	$a = 5.5143(1), c = 13.3680(4)$
$La_{0.7}Sr_{0.3}FeO_{3-\delta}$	LSF	SG	1000	$R\bar{3}c$	$a = 5.5440(2), c = 13.4888(9)$
$La_{0.6}Sr_{0.4}Co_{0.2}Fe_{0.8}O_{3-\delta}$	LSCF$_{0.8}$	SG	900	$R\bar{3}c$	$a = 5.5055(2), c = 13.3908(6)$
$La_{0.6}Sr_{0.4}Co_{0.8}Fe_{0.2}O_{3-\delta}$	LSCF$_{0.2}$	SG	900	$R\bar{3}c$	$a = 5.4479(1), b = 13.2363(6)$
$Ce_{0.8}Gd_{0.2}O_{1.9}$ (buffer)	CGO	Praxair	–	$Fm\bar{3}m$	$a = 5.4278(1)$
NiO-CGO	NiO-CGO	–	–	$Fm\bar{3}m$	$a_{NiO} = 4.1781(1), a_{CGO} = 5.4278(1)$
$Sr_2MgMoO_{6-\delta}$	SMM	FD	1000	$I\bar{1}$	$a = 5.5706(1), b = 5.5749(2),$ $c = 5.5873(2), \alpha = 119.890(2)°,$ $\beta = 119.934(3)°, \delta = 89.955(3)°$
$La_{0.75}Sr_{0.25}Cr_{0.5}Mn_{0.5}O_{3-\delta}$	LSCM	SG	1200	$R\bar{3}c$	$a = 5.4931(1), c = 13.3289(3)$

FD: freeze-drying, SG: sol–gel citrate, Praxair: commercial powders.

Table 2
Sintering temperature (T_d) of the different electrode materials on apatite-type electrolyte. Area-specific resistances (ASR) and activation energies (Ea) for the different electrode materials deposited on as-prepared electrolytes and with a CGO-buffer layer used as protective material between the electrolyte and electrode. ASR values were obtained in air and humidified 5%H_2–Ar for the cathode and anode materials, respectively.

| Composition	T_d (°C)	ASR ($\Omega\,cm^2$)		Ea (eV)	ASR ($\Omega\,cm^2$) CGO-buffer		Ea (eV)
		800 °C	600 °C		800 °C	600 °C	
$La_{0.8}Sr_{0.2}MnO_{3-\delta}$	1100 °C/1 h	5.9	460	1.92	0.16	5.94	1.45
$La_{0.7}Sr_{0.3}FeO_{3-\delta}$	1050 °C/1 h	0.87	62.4	1.71	–	–	–
$La_{0.6}Sr_{0.4}Co_{0.2}Fe_{0.8}O_{3-\delta}$	1000 °C/1 h	0.38	30.9	1.74	–	–	–
$La_{0.6}Sr_{0.4}Co_{0.8}Fe_{0.2}O_{3-\delta}$	950 °C/1 h	0.12	6.6	1.58	0.043	0.654	1.04
$La_{0.75}Sr_{0.25}Cr_{0.5}Mn_{0.5}O_{3-\delta}$ (cathode)	1050 °C/1 h	3.31	216	1.84	0.61	36.5	1.62
NiO-CGO	1300 °C/1 h	0.59	8.44	1.03	0.571	7.14	0.97
$Sr_2MgMoO_{6-\delta}$	1100 °C/1 h	130	1045	1.21	0.87	27.2	1.31
$La_{0.75}Sr_{0.25}Cr_{0.5}Mn_{0.5}O_{3-\delta}$ (anode)	1050 °C/1 h	2.04	14.8	1.10	0.71	12.3	1.09

and high chemical reactivity with the electrodes typically used in SOFC technology [10]. However, these drawbacks can be overcome by operating in the intermediate temperature range (600–800 °C). Indeed, high performances have been obtained with ceria-based electrolytes operating in a SOFC at 600 °C, and doped lanthanum gallates at 800 °C [12,13].

The silicate oxides with apatite-type structure and composition $La_{10-x}(SiO_4)_6O_{2\pm\delta}$ have been also proposed as promising electrolytes for SOFCs, exhibiting high ionic conductivity compared to the YSZ in the intermediate temperature range, combined with moderate thermal expansion coefficients and low electronic conductivity [14–20]. Numerous works, including theoretical atomistic simulations [21–23] and neutron powder diffraction [23–25], show that the ionic conduction occurs mainly via interstitial oxide migration both parallel and perpendicular to the channels [23] and it increases with the oxygen concentration in the lattice.

Silicate apatites present actually several limitations for their potential use in a SOFC as electrolyte. One of the main drawbacks of apatite-type materials resides in the difficulty to prepare dense ceramic materials, which are needed for SOFC operation. On the other hand, degradation of the ionic transport properties with time in reducing atmospheres at high temperatures have been reported for these materials, which was ascribed to silica migration and volatilization in the ceramic surface [26]. The apatite structure allows a large amount of cation substitutions. Among them, the partial substitution of Si^{4+} by Al^{3+} seems to enhance the ionic conductivity and partially suppresses silicon volatilization [27,28].

Despite the number of reports on the structural and transport properties of many apatite electrolytes, their potential use in SOFC devices has not been largely studied [29–33]. In this sense, Tsipis et al. [30] and Yaremchenko et al. [33] reported the electrochemical behaviour of different cathode materials in contact with silicate apatite electrolytes and they found that silicon migration towards the surface layer blocks the electrochemical reaction zones increasing the electrode polarisation [30]. In addition, high area-specific resistances were found by Brisse et al. with NiO-

$La_9SrSi_6O_{26.5}$ cermets [29]. However, a complete single fuel cell with apatite-type electrolyte, using different electrode materials, has not been reported before. Hence, further studies are still needed for a better characterisation of these potential electrolyte materials for SOFCs on several issues, such as the chemical reactivity and electrochemical performance between apatite electrolytes and different electrode materials.
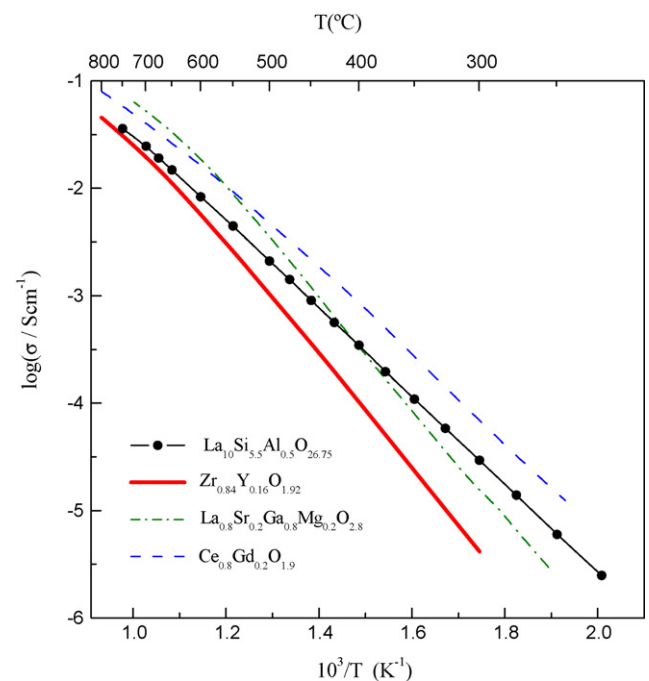
Fig. 1. Arrhenius plot of the overall conductivity of $La_{10}Si_{5.5}Al_{0.5}O_{26.75}$ and different commercial solid electrolyte materials: $Zr_{0.84}Y_{0.16}O_{1.92}$ (Tosoh), $Ce_{0.8}Gd_{0.2}O_{1.9}$ (NexTech) and $La_{0.8}Sr_{0.2}Ga_{0.8}Mg_{0.2}O_{2.8}$ (Praxair).

The aim of this work is to evaluate the potential use of $La_{10}Si_{5.5}Al_{0.5}O_{26.75}$ as a solid electrolyte for SOFCs. Chemical compatibility and area-specific resistance, with several electrode materials, are investigated by X-ray powder diffraction, energy dispersive spectroscopy and impedance spectra measurements. A doped-ceria layer was also used to prevent reactivity between the electrolyte and electrode materials. In addition, a single fuel cell is assembled with the most compatible electrodes to study the fuel cell performance after long term operation.

2. Experimental

2.1. Synthesis and powder characterisation

Polycrystalline powders of $La_{10}Si_{5.5}Al_{0.5}O_{26.75}$ electrolyte were obtained by a freeze-dried precursor method. High purity powders of SiO_2, La_2O_3 and $Al(NO_3)_3 \cdot 9H_2O$ supplied by Aldrich were mixed, pressed into pellets and then calcined at 1300 °C for 5 h. The pellet was ground and the resulting powders were dissolved in diluted nitric acid using a hot-plate with continuous stirring. After that an aqueous stoichiometric cation solution was obtained using ethylenediaminetetraacetic acid as complex agent in a ligand:metal molar ratio of 1:1. The solution was dropped and flash frozen in liquid nitrogen retaining the cation homogeneity of the starting solution. The small ice crystals were dehydrated by vacuum sublimation in a Hetoliolab freeze-drier obtaining a dried and amorphous precursor powder. A single phase was obtained after firing the powders at 1100 °C for 1 h in air. Further experimental details will be reported elsewhere [34].

The electrode materials were prepared by freeze-dried or sol–gel citrate precursor methods (Table 1). The starting reagents were: $La(NO_3)_3 \cdot 6H_2O$ (99.99%), $Sr(NO_3)_2$ (99.9%), $Ca(NO_3)_2 \cdot 4H_2O$ (99%), $Fe(NO_3)_3 \cdot 9H_2O$ (98%), $Mn(NO_3)_2 \cdot 6H_2O$ (99.99%), $Cr(NO_3)_3 \cdot 9H_2O$ (99%), $Ni(NO_3)_2 \cdot 6H_2O$ (99%) and MoO_3 (99.5%), all of them supplied by Aldrich. The corresponding metal nitrates, which are generally hygroscopic, were previously studied by thermogravimetric analysis TG/DTA (Perkin Elmer, mod. Pyris Diamond) to determine the correct cation stoichiometry. The synthesis procedure was similar to that reported previously [35,10,36]. All investigated electrodes were single phases after firing at the temperatures listed in Table 1 without any trace of secondary phases. The cell parameters obtained by the Rietveld refinement at room temperature are consistent with those reported in ICSD database [37]. Commercial powders of $La_{0.8}Sr_{0.2}MnO_{3-\delta}$ (LSM, Praxair specialty ceramics) were also used as cathode material and $Ce_{0.8}Gd_{0.2}O_{2-\delta}$ (CGO) as a protective buffer between electrode and the electrolyte layers. NiO-CGO composite powders, 30 wt.% of CGO, were prepared by adding CGO powders to an ethanol solution of nickel nitrate. The solution was dried under stirring at room temperature and then fired at 900 °C for 1 h to obtain the composite material.
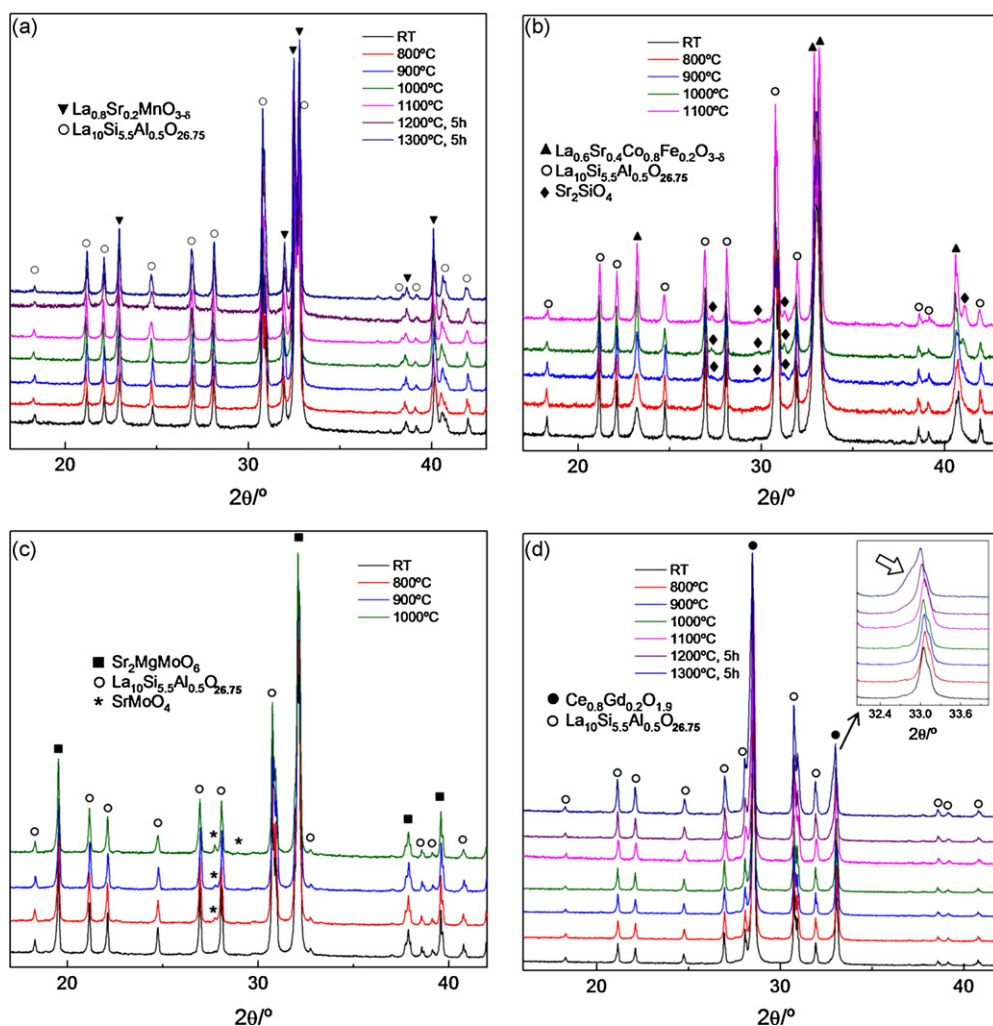

Fig. 2. XRPD patterns for (a) LSM/apatite (b) LSCF0.2/apatite (c) SMM/apatite and (d) CGO/apatite powder mixtures (1:1 wt.%) at room temperature (RT) and after firing between 800 and 1300 °C. The different reaction products when increasing temperature are indicated in the figure.

X-ray powder diffraction (XRPD) patterns were recorded using a PANalytical X'Pert automated diffractometer equipped with the X'Celerator detector and CuKα radiation. The scans were collected in the 2θ range (10–100°) with 0.016° step for 2 h. XRPD studies were also performed to evaluate the chemical compatibility of the apatite-type electrolyte with the different electrodes listed in Table 1. Mixtures of electrolyte and electrodes powders were prepared in a 1:1 (wt.%) ratio, ground in an agate mortar and then fired between 800 and 1300 °C for 5–24 h. The powder mixtures were then cooled to room temperature and investigated by XRPD. Phase identification and quantification were performed with X'Pert HighScore Plus v.2.2d software using the ICSD database for the structural models [37,38]. The usual profile parameters (scale factors, background coefficients, zero-points, pseudo-Voigt and asymmetry parameters for the peak-shape) were refined. The atomic parameters were fixed and not refined.

2.2. Conductivity and area-specific resistance measurements

The polycrystalline powders of $La_{10}Si_{5.5}Al_{0.5}O_{26.75}$ obtained by freeze-dried precursor were uniaxially pressed into disks of 13 mm of diameter and 1 mm of thickness under a pressure of 250 MPa. The green pellets were covered with powders of the same apatite electrolyte and sintered at 1550 °C for 1 h in air, reaching relative densities around 95%. Pt-paste electrodes were painted on each side of the pellet as current collectors. The overall conductivity of the pellets was determined by impedance spectroscopy using a 1260 Solartron FRA in the 0.1–10^6 Hz frequency range from 800 to 250 °C with a cooling rate of 5 °C min^{-1} and stabilisation time of 15 min between consecutive measurements. An ac signal of 50 mV was applied to obtain reproducible spectra.

For area-specific resistance measurements, symmetrical electrodes were coated on both sides of the dense $La_{10}Si_{5.5}Al_{0.5}O_{26.75}$ pellets using a slurry prepared with the different electrode powders and Decoflux^{TM} (WB41, Zschimmer and Schwarz) as binder material. The symmetrical cells were fired, depending on the electrode composition, between 950 and 1300 °C for 1 h in air (Table 2). Afterwards, a Pt-based ink was applied onto the electrodes to obtain a current collector layer and finally fired at 900 °C for 30 min. Symmetrical cells with a CGO-buffer layer between the electrolyte and electrodes, in order to prevent a possible reactivity, were also investigated. The CGO buffer was fixed on as-prepared apatite electrolyte at 1300 °C for 1 h.

The area-specific resistance (ASR) values were obtained under symmetrical atmospheres (air or humidified 5%H$_2$–Ar) in a two electrode configuration. Impedance spectra of the electrochemical cells were collected using the Solartron 1260 FRA, at open circuit voltage (OCV), in the 0.01–10^6 Hz frequency range with an ac signal amplitude of 50 mV. The spectra were fitted to equivalent circuits using the ZView software [39], which allows an estimation of the resistance and capacitance associated with the different contributions. Scanning Electron Microscopy (SEM) images were obtained on a JEOL SM-6490LV electron microscope combined with energy dispersive spectroscopy (EDS) to analyse the microstructure, connectivity between electrodes and electrolyte layers, or any evidence of degradation after tests. The samples for SEM observation were gold or carbon-sputtered in order to avoid charging of the surface.

2.3. Fuel cell tests

Single fuel cells were prepared using 1 mm-thick dense pellets of $La_{10}Si_{5.5}Al_{0.5}O_{26.75}$ as electrolyte with $La_{0.6}Sr_{0.4}Co_{0.8}Fe_{0.2}O_3$ (LSCF0.2) and 70 wt.% NiO-CGO composite as cathode and anode materials, respectively. A CGO-buffer layer was fixed on both sides of the electrolyte at 1300 °C. After that, Ni-CGO anode was fixed at 1300 °C for 1 h on one side of the silicate electrolyte and then

LSCF0.2 cathode was fixed at 950 °C for 1 h on the other side. The electrode surface area was 0.25 cm^2. The sample was sealed against the electrochemical setup using a ceramic-based material (Ceramabond 668, Aremco). Fuel cell tests were carried out using humidified 5%H$_2$–Ar mixture and H$_2$ as fuels and static air as oxidant, operating between 700 and 850 °C. Fuel gases were humidified by bubbling through a gas-washer at a temperature of 20 °C to ensure a constant water content of about 3%. The gas flow fuel rate was set at 100 ml min^{-1}, using a mass-flow controller. Current-voltage (I–V) curves were obtained by cyclic-voltammetry at a scan rate of 5 mV s^{-1} using a Zahner IM6ex unit. The electrochemical tests were performed after reducing the anode material for 1 h in 5%H$_2$–Ar at 800 °C. The stability of the cells was studied for 100 h of operation at 800 °C. Impedance spectra under asymmetrical atmospheres were also acquired at open circuit voltage (OCV) in the frequency range of 0.1 Hz to 1 MHz with an ac perturbation of 50 mV.

3. Results and discussions

3.1. Conductivity

The overall conductivity for $La_{10}Si_{5.5}Al_{0.5}O_{26.75}$ is shown in Fig. 1. For comparison the conductivity data of the most widely used solid electrolytes are also plotted in this figure. As it can
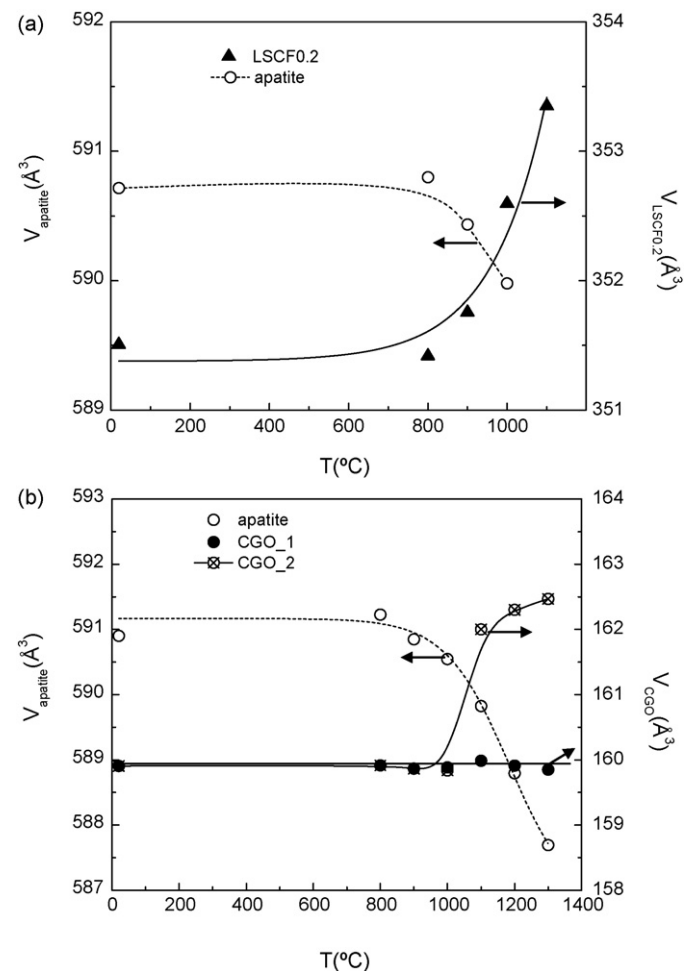

Fig. 3. Variation of the volume cell parameters for the different phases in the (a) LSCF0.2/apatite and (b) CGO/apatite powder mixtures as a function of the sintering temperature.

be observed the conductivity of this apatite oxide is higher than that of YSZ in the whole studied temperature range and especially in the low temperature range. In addition, the values of conductivity of this apatite electrolyte are somewhat lower than those of the lanthanum gallate and ceria-based electrolytes, e.g. $0.025\,S\,cm^{-1}$ for $La_{10}Si_{5.5}Al_{0.5}O_{26.75}$, $0.02\,S\,cm^{-1}$ for $Zr_{0.84}Y_{0.16}O_{1.92}$ (YSZ), $0.041\,S\,cm^{-1}$ for $Ce_{0.8}Gd_{0.2}O_{1.9}$ (CGO) and $0.053\,S\,cm^{-1}$ for $La_{0.8}Sr_{0.2}Ga_{0.8}Mg_{0.2}O_{2.85}$ (LSGM) at $700\,°C$ in air. The conductivity values obtained for $La_{10}Si_{5.5}Al_{0.5}O_{26.75}$ are similar to those obtained previously by Shaula et al. (e.g. $0.028\,S\,cm^{-1}$ at $700\,°C$ [28]). Therefore, the conductivity of this apatite silicate is relatively high, and high performance is expected by using this material as SOFC electrolyte in the intermediate temperature range (600–800 °C).

3.2. Chemical compatibility

The chemical reactivity between the electrolyte and electrode material is an important issue for the SOFC performance. An excessive reactivity between the electrolyte and the electrodes might create new phases, which can increase the ohmic resistance of the cell, blocking the oxygen transference and reducing the electrochemical reaction sites in the electrode–electrolyte interface [40]. An ionically insulating layer could even suppress completely the electrochemical reactions in the electrode–electrolyte interface.

On the contrary, a poor electrode adhesion might result in a larger contact resistances and even delamination of both layers. For these reasons, it is essential to know the chemical compatibility between cell components and the optimum sintering temperature

in order to minimise the possible formation of reaction products at the electrode–electrolyte interfaces.

The chemical compatibility of $La_{10}Si_{5.5}Al_{0.5}O_{26.75}$ was evaluated by XRPD with different electrode materials (Table 1). The XRPD patterns of several apatite-electrode powder mixtures fired between room temperature (RT) and 1300 °C are shown in Fig. 2.

The XRPD patterns of apatite-LSM mixture do not show appreciable structural changes after firing between room temperature and 1300 °C (Fig. 2a). Additional phases are not observed in the patterns at high firing temperatures as 1300 °C. However, the cell volume for apatite-type electrolyte varied from $590.5\,Å^3$ at RT to $591.2\,Å^3$ after firing the mixture at 1300 °C for 5 h, while in the same temperature range the cell volume for LSM varied from 352.0 to $352.6\,Å^3$. The small variation of cell volume of both phases seems to indicate that cation diffusion between both materials is not very significant.

The XRPD patterns of apatite and LSCF0.2 mixture show some additional diffraction peaks above 900 °C, which could be assigned to Sr_2SiO_4 (PDF 024-1231) (Fig. 2b). As expected, the formation of reaction products increases with the firing temperature between 900 and 1100 °C, although its fraction is relatively small compared to the main phases. The cell volume for the apatite shrinkages with the increase of the sintering temperature from 590.7 to $590.0\,Å^3$, while it expands for the LSCF0.2 phase from $351.0\,Å^3$ at RT to $353.5\,Å^3$ at 1100 °C (Fig. 3a). In this case, cobalt is expected to be the main cation incorporating into the apatite structure. In fact, cobalt substitution has been reported in the apatite silicates and Co can be doped in both the Si and La sites [41]. It has been also reported that cobaltite cathodes exhibit high chemical reactivity with most
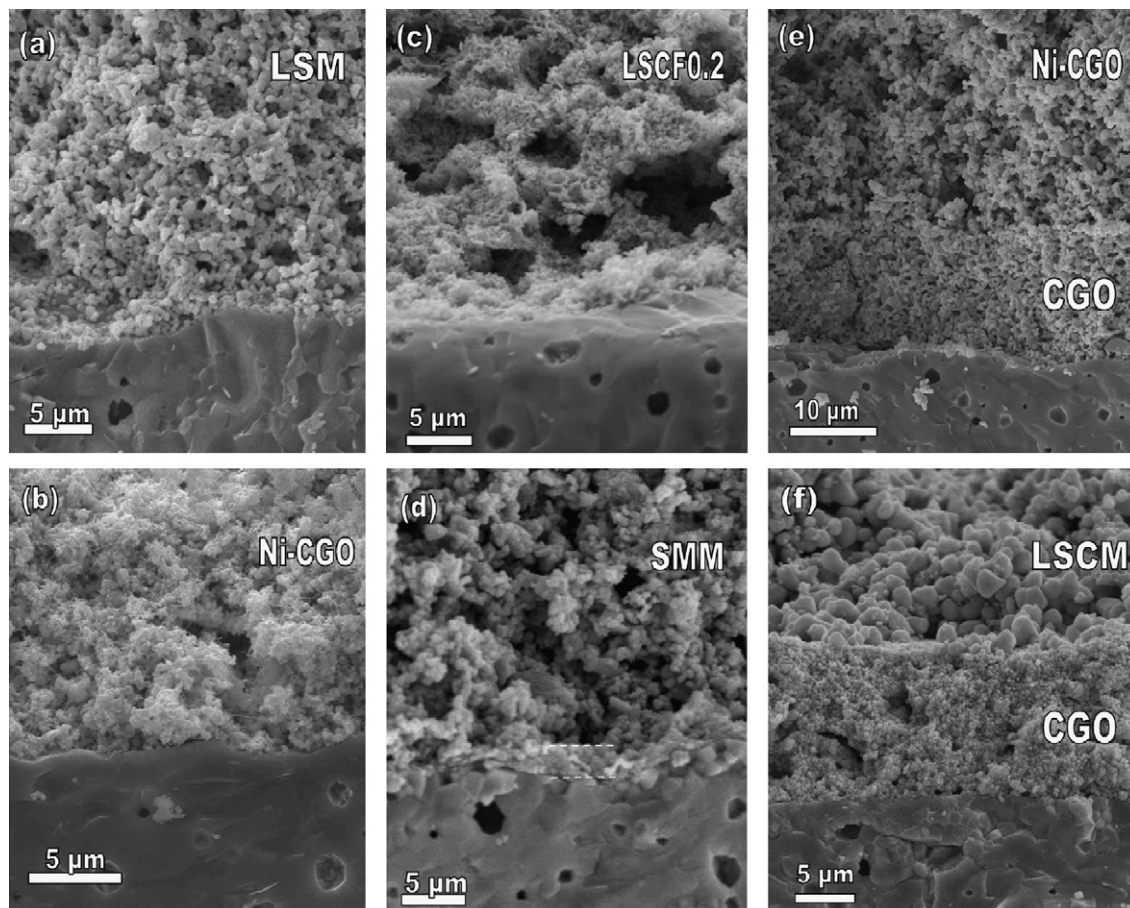

Fig. 4. SEM images of the cross-section at the electrolyte-electrode interfaces: (a) LSM/apatite, (b) Ni-CGO/apatite, (c) LSCF0.2/apatite, (d) SMM/apatite, (e) Ni-CGO/CGO/apatite and (f) LSCM/CGO/apatite.

electrolytes, such as YSZ, CGO and LSGM above 1000 °C. The cobalt migration towards the electrolyte at high sintering temperatures is the main origin of this chemical reactivity [1,2].

The XRPD patterns for the apatite and the double perovskite SMM mixture show that these phases react from just 800 °C being the scheelite-type $SrMoO_4$ the reaction product (Fig. 2c). Despite the fact that the fraction of $SrMoO_4$ is not significant up to 1000 °C, the insulating nature of this material and its segregation at the electrode/electrolyte interface could affect negatively to the performance of the fuel cell. It should be mentioned that high chemical reactivity has been also observed between SMM and several electrolytes, such as YSZ and LSGM, and the main reaction product was $SrMoO_4$ [42]. In fact, a ceria buffer between SMM and LSGM was necessary to prevent reactivity and to achieve high efficiency [42,43].

The reactivity between this apatite electrolyte and CGO was also investigated. This last phase was used as protective buffer layer between the silicate electrolyte and the different electrode materials. The XRPD patterns for apatite-CGO mixture do not show evidence of bulk reactivity below 1000 °C (Fig. 2d). However, the diffraction peaks for CGO become asymmetric at high firing temperatures. This is more clearly visible in the inset of Fig. 2a, where all the diffraction peaks of the fluorite structure exhibit at least two components above 1000 °C, indicating cation interdiffusion between fluorite and apatite structures. The XRPD patterns were analyzed by Rietveld method, considering three phases: the apatite and two fluorite-type structures with similar cell parameters. The variation of the cell parameters in the mixture as a function of the firing temperature (Fig. 3b) shows that the volume cell for the apatite decreases with increasing temperature. On the contrary, it remains almost constant for the main fluorite-type phase and it

increases for the other additional fluorite phase. Since the cell volume for $La_{10-x}Si_{5.5}Al_{0.5}O_{26.5}$ series decreases with the lanthanum deficiency and the cell volume in $Ce_{1-y}La_yO_{2-\delta}$ increases with lanthanum doping [1,2]. The lanthanum interdiffusion from apatite into fluorite structure could explain this behaviour. It should be noted that the diffusion of lanthanum into the CGO structure occurs at very high firing temperatures, so that this effect is reduced operating at low temperature.

Chemical compatibility between NiO and the apatite electrolyte (XPRD not presented here) were also performed and additional phases were not observed even up to 1300 °C. The cell volume remains almost constant, varying from 72.93 to 73.00 Å³ for NiO and from 590.6 to 591.2 Å³ for the apatite electrolyte in the temperature range RT–1300 °C.

Considering the low chemical reactivity between the silicate electrolyte and these electrodes, even at very high firing temperatures, one should expect high performance of these electrodes in contact with the silicate electrolyte operating in a SOFC. However, minor secondary phases or interdiffusion at the electrode/electrolyte interface may have negative effects on the cell performance as aforementioned. The study of the area-specific resistance and serial resistance obtained from symmetrical cells is an useful method to determine the influence of the interfacial reaction between the different material layers of the cell.

3.3. Microstructure of the symmetrical cells

The different electrode materials were sintered on the apatite electrolyte at the lower possible temperature to ensure an adequate adherence, but avoiding excessive chemical reaction between the components. The sintering temperatures used for the different
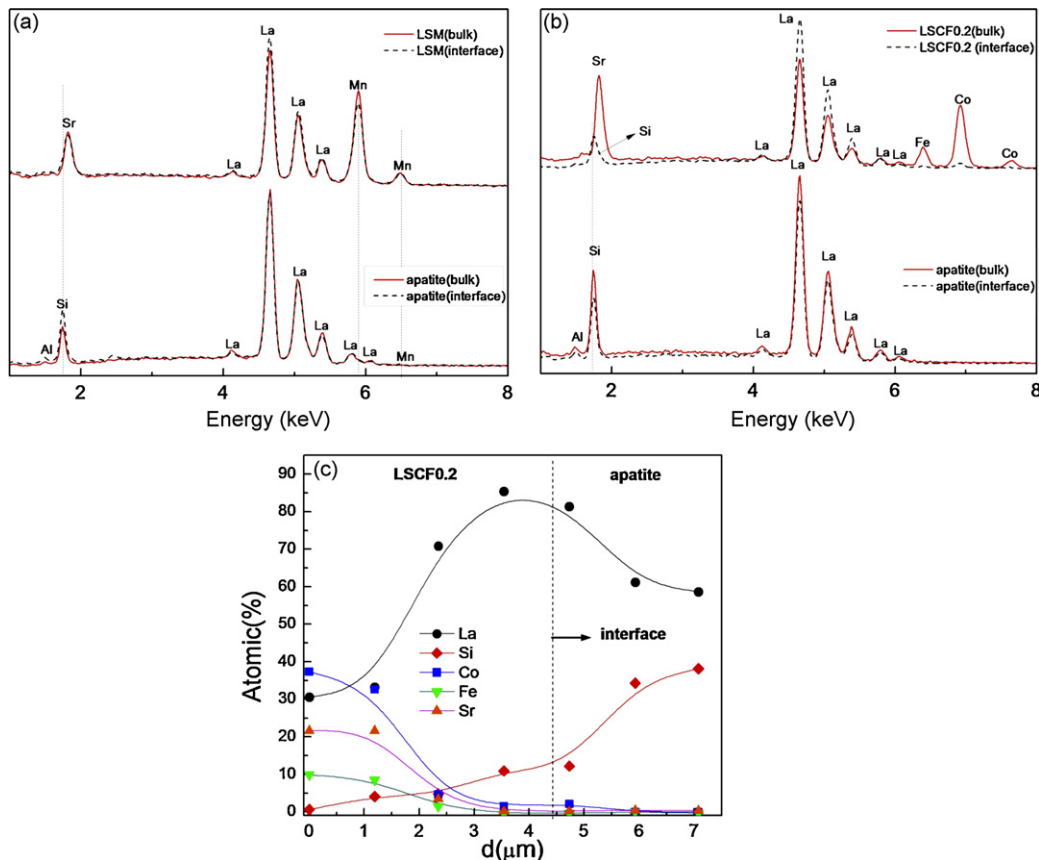

Fig. 5. EDS spectra of (a) LSM/apatite and (b) LSCF0.2/apatite in the bulk and near the electrolyte and electrode interface. (c) Variation of the atomic fraction for LSF0.2/apatite with the distance to the interface.

electrodes are given in Table 2. Fig. 4 shows representative SEM images corresponding to the electrode/electrolyte interfaces of several symmetrical cells after the electrochemical tests. All electrode layers present adequate porosity and apparently good adherence with the electrolyte layer. The thickness of the electrodes varied in the range 25–35 μm.

The LSM/apatite (Fig. 4a), Ni-CGO/apatite (Fig. 4b) and LSCF0.2/apatite (Fig. 4c) cells did not show appreciable reactivity at their interfaces. In contrast, a small interdiffusion region is observed in the SMM/apatite interface (Fig. 4d), similar to that found in the SMM/LSGM interface studied in a previous work [42], which was associated with molybdenum migration from the electrode towards the electrolyte interface. The CGO buffer sintered on apatite electrolyte at 1300 °C is porous and it has a thickness of 10–15 μm (Fig. 4e and f).

EDS measurements at the electrode/electrolyte interface were performed (Fig. 5). Cobalt, manganese, strontium and/or iron diffusion into the electrolyte were not detected (Fig. 5a and b), considering the experimental errors of the technique, which is estimated to be about 1–2%. This seems to confirm the results obtained by XRD analysis, where significant bulk reactivity was not detected. However, lanthanum and silica migration at the electrode/electrolyte interface were observed in several interfaces. As an example, Fig. 5c shows the variation of atomic concentration with the distance at the LSCF0.2/apatite interface estimated by EDS. A La-rick region was observed near the interface and a small fraction of silica diffuses towards the cathode layer. The diffusion of silica was detected in a region of 2–4 μm towards the cathode materials, however, this is not detectable by XRPD due to the small amount and also possibly amorphous state, as also previously suggested by Tsipis et al. [30].

3.4. Electrode polarisation and serial resistance of the symmetrical cells

Representative impedance spectra of symmetrical cells are shown in Figs. 6 and 7. The spectra were fitted using equivalent circuits to obtain the resistance and capacitance of each contribution. The equivalent circuits consisted of a serial association of (RQ) elements attributed to electrolyte or electrode processes, where R is a resistance and Q is a constant phase element. The constant phase element with impedance $Z = (jwQ)^{-n}$ is related to the ideal capacitance by:

$$C_i = \frac{(R_i Q_i)^{1/n}}{R_i} \tag{1}$$

Additionally, the relaxation frequency f is related to the constant phase element and resistance by:

$$f = \frac{1}{2\pi RC} = \frac{1}{2\pi (R_i Q_i)^{1/n}} \tag{2}$$

In the high temperature range ($T > 650$ °C) only electrode processes are observed and the impedance spectra were fitted with the following equivalent circuit: $LR_s(RQ)_{HF}(RQ)_{LF}$, where L is an autoinductance attributed to the equipment, R_s is the serial resistance associated with the overall ohmic losses of the symmetrical cell and the subscript HF and LF denote the high and low frequency electrode processes, respectively (Fig. 6). In the low temperature range ($T \leq 650$ °C), electrolyte contributions are observed and the following equivalent circuit was considered for the fitting: $(RQ)_{GB}(RQ)_{HF}(RQ)_{LF}$, where the subscript GB denotes the grain boundary process (Fig. 7). Only the overall polarisation resistance are considered here, which were obtained from the addition of the each polarisation contribution R_i. The parameters obtained by fitting the impedance spectra are given as supplementary content in Table S1 and S2 for some electrodes at different temperatures.
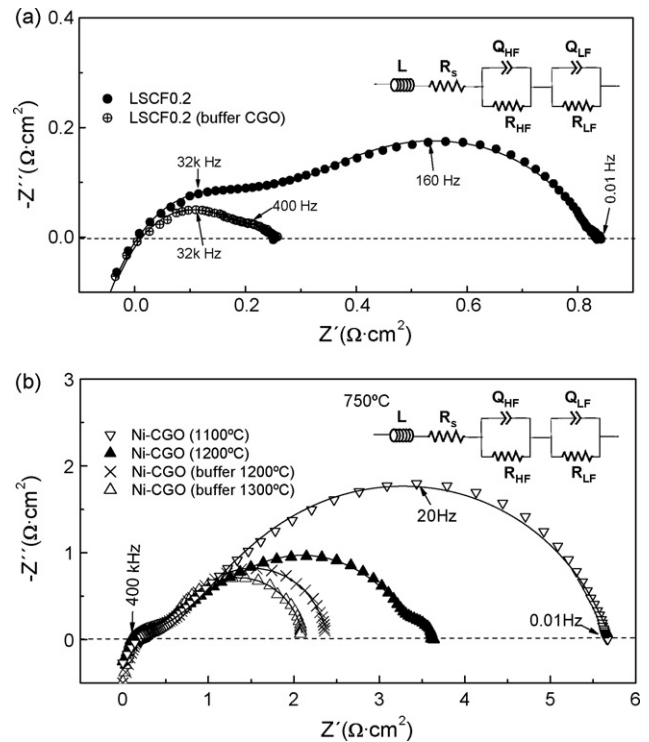

Fig. 6. Impedance spectra of (a) LSCF0.2 cathode (air) and (b) Ni-CGO (5%H₂–At) anode in contact with the as-prepared apatite-type electrolyte and with a CGO-buffer layer between the anode and the electrolyte layers at 750 °C. The Ni-CGO electrodes were fixed at different temperatures as indicated in the figure. The solid line is the fitting result obtained with the equivalent circuits. The serial resistance was subtracted for better comparison of the spectra.

The temperature dependence of the area-specific resistance (ASR) in static air for the different cathodes is shown in Fig. 8a. The manganite LSM and chromium-manganite LSCM, fixed on apatite electrolyte at 1100 °C, exhibit the highest ASR values, i.e. 3–6 Ω cm² at 800 °C (Table 2). It should be commented that these values are comparable to that reported by Tsipis et al. for 40%CGO-LSM ~5.5 Ω cm² at the same temperature [30]. Notice that ASR values for LSM and LSCM increase as the electrode sintering temperature increases. These high values of ASR cannot be ascribed to a significant bulk reactivity between the electrolyte and the cathode materials, because this is ruled out by the XRPD analysis. On the other hand, the ohmic resistance of the symmetrical cell would be comparable to the electrolyte resistance if not significant chemical interaction occurs between the different components. In the case of LSM/apatite cell, the serial resistance does not vary appre-
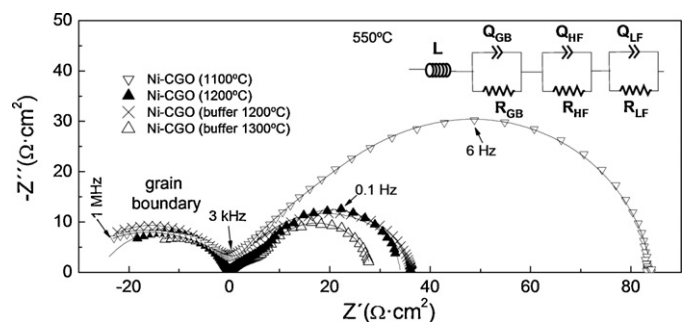

Fig. 7. Impedance spectra of a Ni-CGO anode fixed at different temperatures on apatite electrolyte without and with CGO-buffer layer at 550 °C. The grain boundary process of the electrolyte is observed at high frequency. The serial resistance was subtracted for better comparison of the spectra.
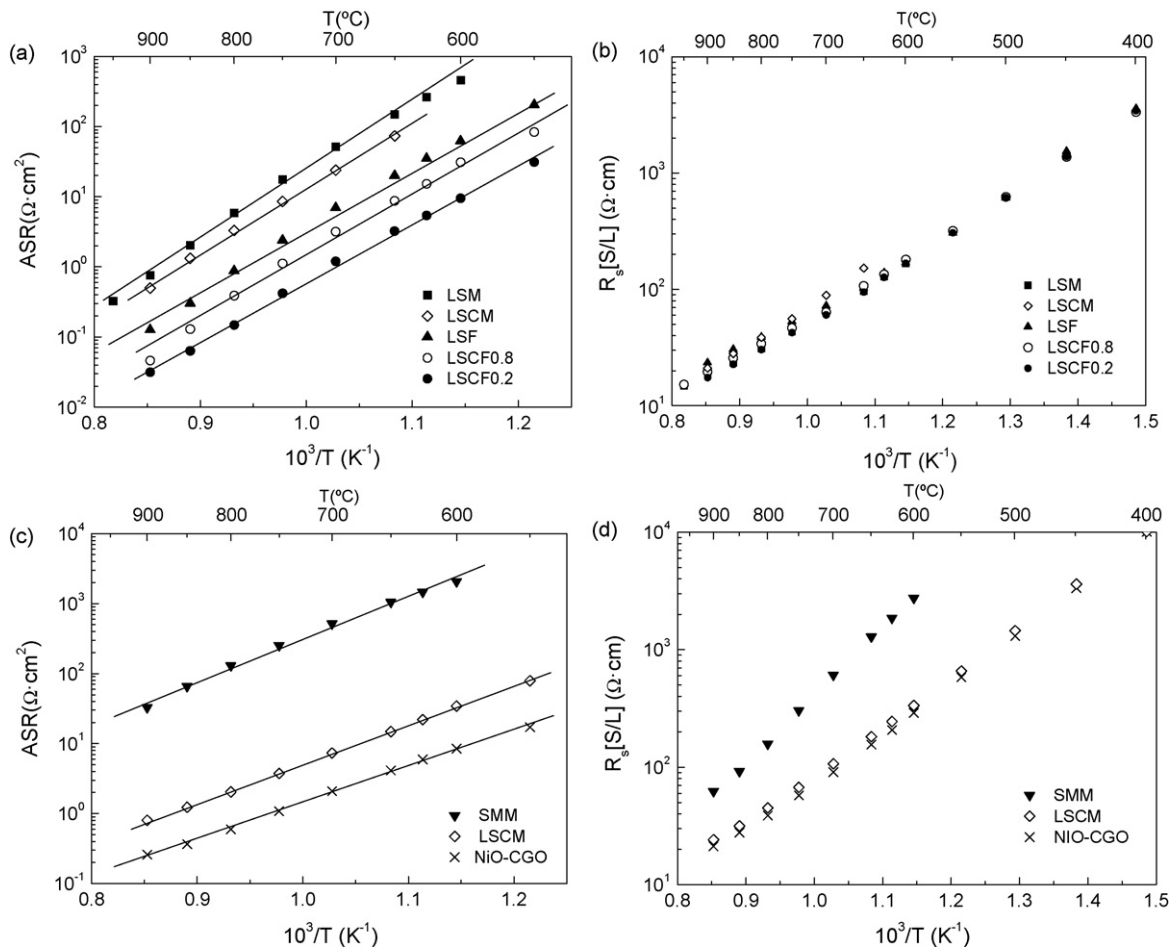
Fig. 8. Area-specific resistance (ASR) values for the different (a) cathode and (c) anode materials in contact with apatite electrolyte at open circuit voltage. Overall serial resistance of the symmetric cells for the different (b) cathode and (d) anode materials.

ciably compared to the other cells (Fig. 8b), therefore, one can consider that the high polarisation values are ascribed to interfacial reactivity at the electrode/electrolyte interface. High polarisation resistances were also observed by Yaremchenko et al. in several manganese-containing cathodes [33]. This seems to indicate that manganese-based electrodes are not chemically compatible in contact with silicates and the diffusion of silica and/or manganese at the interface increase the electrode polarisation.

Ferrites and cobalt-ferrites based cathodes exhibit lower ASR values in contact with apatite electrolyte compared to manganite-based materials (Table 2). However, these cathodes were fixed at somewhat lower temperature compared to LSM and lower reactivity at the electrode/electrolyte interface is expected. The lowest ASR values correspond to LSCF0.2, typically less than $0.12\,\Omega\,cm^2$ at 800 °C after sintering at 950 °C for 1 h (Table 2). This is correlated with the higher mixed ionic-electronic conduction in cobaltite cathodes compared to ferrite and manganite-based materials. However, these ASR values increase with the sintering temperature, although they are always lower compared to those of LSM. It should be also considered that cobalt-ferrites exhibit high thermal expansion coefficient values compared to silicate apatites, however, composites of LSCF and CGO could be used in order to match the thermal expansion coefficient between these components.

The variation of serial resistance with the temperature indicates that the ohmic losses of the cells are almost the same for all investigated electrodes (Fig. 8b). This seems to indicate that the reaction depth is limited at the electrode/electrolyte interface as observed by EDS analysis, although it results in surface limitations as previously suggested by Tsipis et al. with different cathode materials [30].

The activation energies for the temperature dependence of ASR vary from 1.58 eV for LSCF0.2 to 1.92 eV for LSM (Table 2).

The temperature dependence of ASR values in humidified $5\%H_2$–Ar for the different anode materials are shown in Fig. 8c. The double perovskite SMM in contact with silicate electrolyte exhibits very high ASR values, higher than $100\,\Omega\,cm^2$ at 800 °C. This poor ASR values can be associated with the reactivity observed by SEM at the SMM/apatite interface. An additional contribution is observed in the impedance spectra of this cell (not shown) with a capacitance value similar to that of the grain boundary $\sim 10^{-9}\,F\,cm^{-1}$, which seems to be ascribed to an interfacial reaction layer. As a consequence, the overall serial resistance of this cell increases significantly compared to the other electrodes investigated here (Fig. 8d). It should be noted that a significant increase of the serial resistance was also observed in SMM/LSGM symmetrical cells when sintered above 1100 °C [42]. The lowest ASR values are found for NiO-CGO composite i.e. $0.59\,\Omega\,cm^2$ at 800 °C and $8.4\,\Omega\,cm^2$ at 600 °C in humidified $5\%H_2$–Ar. These values of ASR are much lower than those reported by Brisse et al. for NiO-La$_9$SrSi$_6$O$_{26+\delta}$ composites, i.e. $144\,\Omega\,cm^2$ at 600 °C [29].

3.5. Electrode polarisation using a CGO-buffer layer

A CGO-buffer layer was used between the electrolyte and the electrodes to prevent reactivity at the electrode/electrolyte interface. A porous CGO buffer of 15 μm of thickness was sintered on the
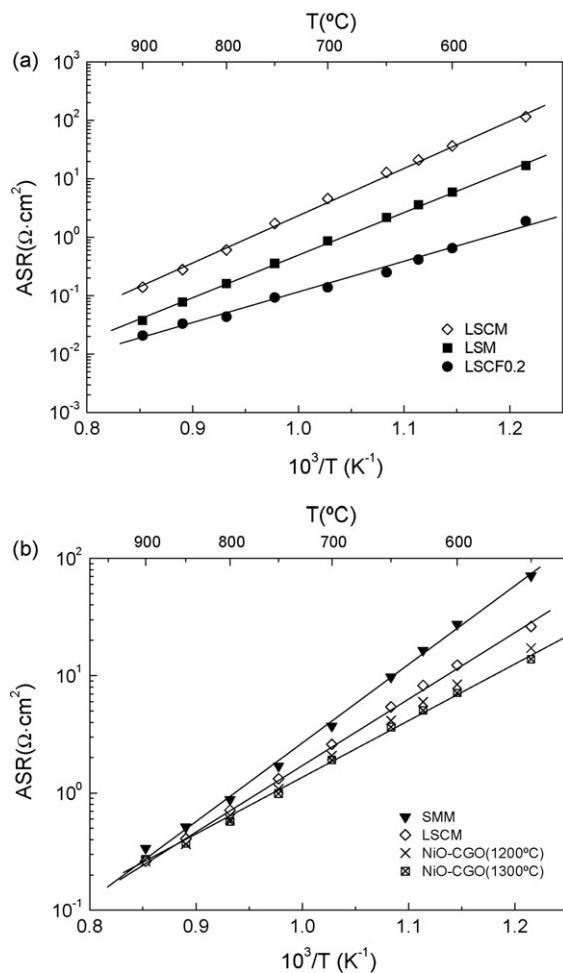
Fig. 9. Area-specific resistance (ASR) values for the different (a) cathode and (b) anode materials with a protective CGO-buffer layer between electrolyte and electrodes at open circuit voltage.

apatite electrolyte at 1300 °C for 1 h (Fig. 4e and f). Then the electrodes were fixed at the sintering temperature given in Table 2. As it can be observed the ASR values for the cathode materials are significantly improved with the CGO-buffer layer (Fig. 9a). For example, the ASR values for LSM decrease from 5.9 to 0.16 Ω cm^2 at 800 °C in air. The lowest ASR values are found again for the cobalt-ferrite LSFC0.2 with a value of only 0.043 Ω cm^2 at 800 °C. The impedance spectra for the symmetrical cells LSCF0.2/apatite comprise two separated contributions in the high temperature range (Fig. 6a). The capacitance values are the order of 4×10^{-5} and 2×10^{-3} F cm^{-2} for the high and low frequency arcs respectively, which indicates that these arcs correspond to charge transfer processes [40]. By comparing the spectra of Fig. 6a one can observe that the arc corresponding to the high frequency contribution is not affected by the use of CGO buffer, while in contrast, the low frequency arc decreases considerably.

The ASR values for SMM and LSCM anode materials also improved when a CGO buffer is used (Fig. 9b). For instance, the ASR values for SMM decrease from 130 to 0.87 Ω cm^2 at 800 °C under humidified 5%H$_2$–Ar mixture (Table 2).

The impedance spectra for NiO-CGO/apatite cells consist of at least two contributions associated with electrode processes (Fig. 6b), and the arc at low frequency is dominant in the whole temperature range studied. The capacitance of this low frequency arc increases with the temperature from 0.07 F cm^{-2} at 550 °C to 0.7 F cm^{-2} at 800 °C, which seems to indicate that this corresponds

to diffusion or adsorption processes (Table S1 and S2, supplementary content). For the high frequency arc the capacitance is around 4×10^{-3} F cm^{-2} at 550 °C and it can be assigned to charge transfer processes [40]. As it can be observed the ASR values for NiO-CGO composites are only slightly improved when a CGO-buffer layer is used (e.g. it varies from 0.59 to 0.57 Ω cm^2 at 800 °C in 5%H$_2$–Ar). It should be also noted that the ASR values for NiO-CGO composite decreases as the sintering temperature increases (Fig. 6b). This is possibly due to a better connectivity between the CGO and NiO grains, because high firing temperatures are usually required to obtain high performance with this composite anode [1,2,4]. The activation energies also decrease slightly if the CGO-buffer layer is used (Table 2). These results suggest that the CGO layer avoids reactivity with the electrodes, improving their efficiency with the silicate electrolyte. In addition, the interdiffusion observed by XRPD between the apatite and CGO seems not to affect significantly the overall serial resistance of the cell in the high and intermediate temperature range, indeed similar values of serial resistance were obtained for the NiO-CGO/CGO/apatite cells sintered between 1100 and 1300 °C. However, an increase of the overall serial resistance is observed in the low temperature range, which is probably related to the ohmic losses of the porous buffer of ceria. One should expect better results if a thin and dense CGO-buffer layer is used.

3.6. Fuel cell tests

A solid oxide fuel cell was assembled with those electrodes exhibiting the lowest ASR values in the symmetrical cells and it was tested with oxidant and fuel gases. NiO-CGO and LSCF0.2 were chosen as anode and cathode materials, respectively. A CGO-buffer layer was used as protective material between the electrolyte and electrodes, although this may be not necessary in case of the anode material, because chemical reactivity was not observed between NiO-CGO and the apatite electrolyte from XRPD and ASR measurements. The *I–V* and performance curves for LSCF0.2/CGO/apatite/CGO/NiO-CGO cell at different temperatures, using air as oxidant and humidified (3%H$_2$O) H$_2$ as fuel, are shown in Fig. 10a. The open circuit voltage obtained (OCV = 1.09 V) is close to the value predicted by the Nernst equation. Maximum power densities of 195 and 65 mW cm^{-2} were reached at 850 and 700 °C respectively, using an 1-mm thick electrolyte and electrode surface area of 0.24 cm^2. It should be commented that the values of power densities are relatively low due to the thickness of the electrolyte used ($\sim$1 mm). The impedance spectra of the cell were acquired at open circuit voltage (Fig. 10b). Two main contributions are visible in these spectra. Taking into account the ASR results, the dominant contribution at high frequency with a capacitance value of 0.1 F cm^{-2} could be mainly ascribed to the anode response, whilst the low frequency contribution with lower capacitance of 1.6×10^{-4} F cm^{-2} is possible assigned to the cathode contribution. The overall electrode polarisation resistances take values of 0.23 Ω cm^2 at 850 °C and 0.84 Ω cm^2 at 700 °C (Fig. 10b).

An approximate expression for the power density is given by the following relation [1]:

$$P = \frac{(OCV)^2}{4R} \tag{3}$$

where OCV is the open circuit voltage (1.1 V at 800 °C in H$_2$), and $R = R_{\Omega} + R_{\eta}$ is the overall resistance of the cell, including ohmic losses R_{Ω} and polarisation resistance R_{η}. The overall cell resistance was obtained from the slope of the linear fitting of the *I–V* curves and the polarisation resistance was determined separately by impedance spectroscopy. Assuming an electrolyte thickness of 100 μm, the power densities obtained would be 840 mW cm^{-2} at 850 °C and 240 mW cm^{-2} at 700 °C from the relation (3). Hence, high power density could be obtained using thin layers of apatite-
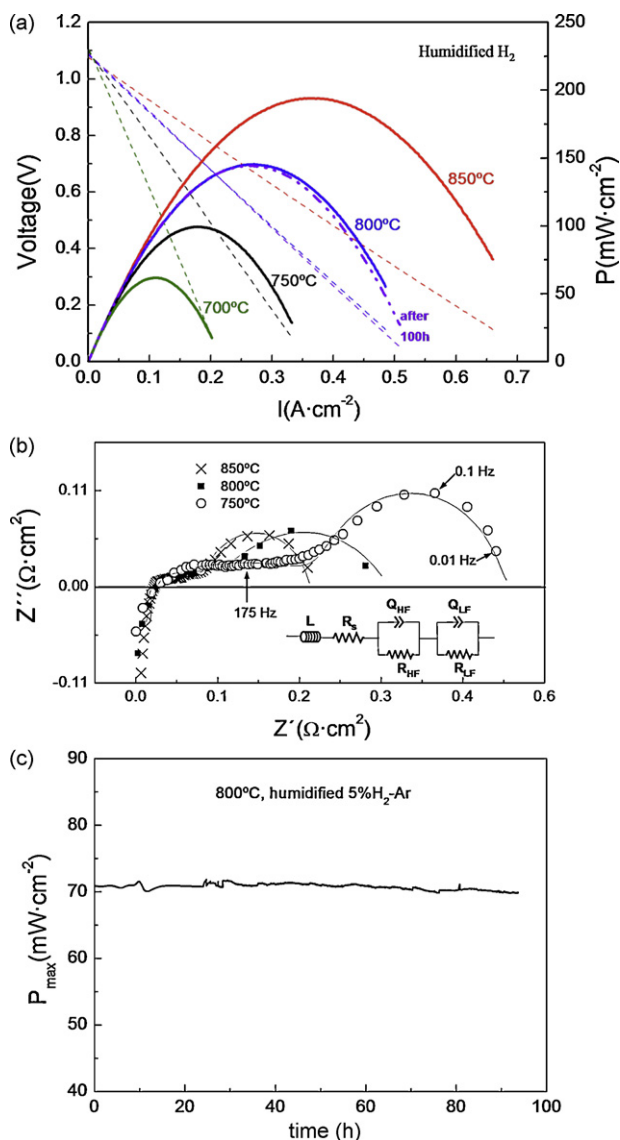
Fig. 10. (a) Cell voltage and power density as a function of current density at different temperatures using air and humidified H$_2$ as oxidant and fuel, respectively, (b) impedance spectra of the overall polarisation resistance for the LSCF0.2/CGO/apatite/CGO/NiO-CGO cell. (c) Variation of maximum power density for 100 h of operation at 800 °C in humidified 5%H$_2$–Ar.

type electrolytes in the intermediate temperature range. The fine apatite powder obtained by freeze-drying method could be used to obtain thin apatite electrolyte layers by using alternative processing methods, such as tape-casting. Although it requires further studies to optimise the composition of the slurries and this is not the aim of this study. In addition, alternative cathodes materials are still required to avoid the use of the ceria buffer, which complicates the fuel cell design and processing. Yarenchemco et al. have recently proposed the use of lanthanum nickelates, e.g. La$_2$NiO$_4$, as possible cathode compatible with apatite silicates, which could avoid the use of ceria buffer.

The stability of the cell was studied for 100 h at 800 °C using humidified 5% H$_2$–Ar as fuel for safety reasons. Stable values of power densities of 70 mW cm^{-2} and OCV were obtained during cell operation (Fig. 10c). Power density curves achieved the same maximum power density after 100 h of operation, using pure hydrogen at 800 °C (Fig. 10a). Thus, appreciable degradation of the fuel cell did not occur during cell operation in these conditions. This seems to indicate that the CGO buffer prevents reactivity of the apatite

with the electrodes and also possible migration of silica towards the electrolyte interface, archiving stable values of performance with time.

4. Conclusions

The compatibility and electrochemical performance of the silicate apatite-type electrolyte, La$_{10}$Si$_{5.5}$Al$_{0.5}$O$_{26.75}$, with several electrode materials frequently used in SOFC were investigated. This electrolyte has conductivity values higher than those of YSZ and comparable to most important solid electrolytes proposed for the intermediate temperature range, such as doped ceria and lanthanum gallate-based electrolytes. Chemical compatibility carried out by XRPD did not reveal appreciable bulk reactivity between silicate and many electrodes up to 1300 °C. EDS analysis showed lanthanum and silica migration towards the electrolyte/electrode interface. The area-specific resistances of the electrodes in contact with the silicate electrolyte were rather high even at low sintering temperatures. These values also increase with the sintering temperature. This suggests that cation interdiffusion blocks the charge transfer reactions at the interface between the apatite electrolyte and electrode materials. This reactivity seems to be higher with manganese-containing materials. On the other hand, the overall serial resistance of the cells is not affected by the chemical interaction, indicating that interdiffusion of elements occurs only at the interface. Lower ASR values are obtained using a protective buffer layer of CGO between the electrolyte and electrode materials. The LSCF0.2/CGO/apatite/CGO/NiO-CGO cell achieved a maximum power density and electrode polarisation of 195 mW cm^{-2} and 0.23 Ω cm^2 at 850 °C, using an electrolyte thickness of 1 mm. Maximum power densities of 840 mW cm^{-2} at 850 °C may be expected using 100-μm thick electrolyte layers.

Appendix A. Supplementary data

Supplementary data associated with this article can be found, in the online version, at doi:10.1016/j.jpowsour.2009.11.068.

References

[1] N.Q. Minh, T. Takahashi, Science and Technology of Ceramic Fuel Cells, Elsevier Science, Amsterdam (Netherlands), 1995.
[2] S.C. Singhal, K. Kendall, High Temperature Solid Oxide Fuel Cells: Fundamental, Design and Applications, Elsevier, Oxford, 2004.
[3] B.C.H. Steele, A. Heinzel, Nature 414 (2001) 345.
[4] R. Mark Ormerod, Chem. Soc. Rev. 32 (2003) 17.
[5] M. Mogensen, N.M. Sammes, G.A. Tompsett, Solid State Ionics 129 (2000) 63.
[6] M. Gödickemeier, L.J. Gauckler, J. Electrochem. Soc. 145 (1998) 414.
[7] V.V. Kharton, F.M.B. Marques, A. Atkinson, Solid State Ionics 174 (2004) 135.
[8] T. Ishihara, H. Matsuda, Y. Takita, J. Am. Chem. Soc. 116 (1994) 3801.
[9] P. Lacorre, F. Goutenoire, O. Bohnke, R. Retoux, Nature 404 (2000) 856.
[10] D. Marrero-López, J. Peña-Martínez, J.C. Ruiz-Morales, D. Pérez-Coll, M.C. Martín-Sedeño, P. Núñez, Solid State Ionics 178 (2007) 1366.
[11] J.W. Stevenson, T.R. Armstrong, L.R. Pederson, J. Li, C.A. Levinsohn, S. Baskaran, Solid State Ionics 113 (1998) 571.
[12] J. Peña-Martínez, D. Marrero-López, J.C. Ruiz-Morales, C. Savaniu, P. Núñez, J.T.S. Irvine, Chem. Mater. 18 (2006) 1001.
[13] Z. Shao, S.M. Haile, Nature 431 (2004) 170.
[14] S. Nakayama, T. Kageyama, H. Aono, Y. Sadaoka, J. Mater. Chem. **5** (1995) 1801.
[15] H. Arikawa, H. Nishiguchi, T. Ishihara, Y. Takita, Solid State Ionics 136–137 (2000) 31.
[16] E.J. Abram, D.C. Sinclair, A.R. West, J. Mater. Chem. 11 (2001) 1978.
[17] J.E.H. Sansom, D. Richings, P.R. Slater, Solid State Ionics 139 (2001) 205.

[18] S. Nakayama, M. Sakamoto, M. Higuchi, K. Kodaira, M. Sato, S. Kakita, T. Suzuki, K. Itoh, J. Eur. Ceram. Soc. 19 (1999) 507.
[19] P.R. Slater, J.E.H. Sansom, J.R. Tolchard, Chem. Rec. 4 (2004) 373.
[20] L. León-Reina, E.R. Losilla, M. Martínez-Lara, S. Bruque, M.A.G. Aranda, J. Mater. Chem. 14 (2004) 1142.
[21] J.R. Tolchard, M.S. Islam, P.R. Slater, J. Mater. Chem. 13 (2003) 1956.
[22] M.S. Islam, J.R. Tolchard, P.R. Slater, Chem. Commun. (2003) 1486.
[23] E. Kendrick, M.S. Islam, P.R. Slater, Chem. Commun. (2008) 715.
[24] L. León-Reina, J.M. Porras-Vázquez, E.R. Losilla, M.A.G. Aranda, Solid State Ionics 177 (2006) 1307.
[25] L. León-Reina, J.M. Porras-Vázquez, E.R. Losilla, D.V. Sheptyakov, A. Llobet, M.A.G. Aranda, Dalton Trans. (2007) 2049.
[26] A.A. Yaremchenko, A.L. Shaula, V.V. Kharton, J.C. Waerenborgh, D.P. Rojas, M.V. Patrakeev, F.M.B. Marques, Solid State Ionics 171 (2004) 51.
[27] A.L. Shaula, V.V. Kharton, F.M.B. Marques, Solid State Ionics 177 (2006) 1725.
[28] A.L. Shaula, V.V. Kharton, F.M.B. Marques, J. Solid State Chem. 178 (2005) 2050.
[29] A. Brisse, A.-L. Sauvet, C. Barthet, S. Beaudet-Savignat, J. Fouletier, Fuel Cell 6 (2006) 59.
[30] E.V. Tsipis, V.V. Kharton, J.R. Frade, Electrochim. Acta 52 (2007) 4428.
[31] H. Yoshioka, Y. Nojiri, S. Tanase, Solid State Ionics 179 (2008) 2165.
[32] C. Bonhomme, S. Beaudet-Savignat, T. Chartier, P.-M. Geffroy, A.-L. Sauvet, J. Eur. Ceram. Soc. 29 (2009) 1781.
[33] A.A. Yaremchenko, V.V. Kharton, D.O. Bannikov, D.V. Znosak, J.R. Frade, V.A. Cherepanov, Solid State Ionics 180 (2009) 878.
[34] D. Marrero-López et al., manuscript in preparation.
[35] J. Peña-Martínez, D. Marrero-López, J.C. Ruiz-Morales, B.E. Buergler, P. Núñez, L.J. Gauckler, J. Power Sources 159 (2006) 914.
[36] D. Marrero-López, J. Peña-Martínez, J.C. Ruiz-Morales, D. Pérez-Coll, M.A.G. Aranda, P. Núñez, Mater. Res. Bull. 8–9 (2008) 2441.
[37] Inorganic Crystal Structure Database (ICSD) v2008-02.
[38] X'Pert HighScore Plus, version 2.2d, PANalytical BV 2004.
[39] D. Johnson, ZView: a Software Program for IES Analysis, Version 2.8, Scribner Associates, Inc. Southern Pines, NC, 200.
[40] S.B. Adler, Chem. Rev. 104 (2004) 4791.
[41] J.R. Tolchard, J.E.H. Sansom, M.S. Islam, P.R. Slater, Dalton Trans. 20 (2005) 1273.
[42] D. Marrero-López, J. Peña-Martínez, J.C. Ruiz-Morales, M. Gabas, P. Núñez, M.A.G. Aranda, J.R. Ramos-Barrado, doi:10.1016/j.ssi.2009.11.005.
[43] Y.H. Huang, R.I. Dass, Z.L. Xing, J.B. Goodenough, Science 312 (2006) 254.